Rev.Adv.Mater.Sci. 13 (2006) 59-70

BRIDGING THE GAP BETWEEN COMPUTATIONAL AND EXPERIMENTAL LENGTH SCALES: A REVIEW ON NANO-SCALE PLASTICITY

Julia R. Greer

PARC, Palo Alto Research Center, Electronic Materials and Devices Laboratory
3333 Coyote Hill Road, Palo Alto, CA 94304, USA

Received: August 15, 2006

Abstract. The results of both experimental studies and molecular dynamics simulations indicate that crystals exhibit strong size effects at the sub-micron scale: smaller is stronger. Until recently, experimental aspects of nano-scale deformation involved the effects of strain gradients, constraints of neighboring layers, grain boundaries, etc., which were key factors in observed size effects. Even without experimental constraints, many computational studies find that yield strength depends on sample size through a power relationship. Both experimental and computational results suggest that a fundamentally different plasticity mechanism might operate at the length scale of material's microstructure. In this work a brief review of some of these works is presented and compared with the results of our gold nanopillar micro-compression experiments, which were found to deform at nearly 50% of theoretical shear strength. To explain the observed size effect, we introduce our phenomenological model of hardening by dislocation starvation.

1. INTRODUCTION

While 'super-sizing' seems to be the driving force of our food industry, the direction of materials research has been quite the opposite: the dimensions of many technological devices are becoming ever smaller each year. This continuous reduction in size drives a great demand for understanding the mechanical behaviour, and in particular, the strength of materials at the sub-micron scale. In bulk form, the yield stress and strength of the material remain nearly constant regardless of the sample size because the sample dimensions are large compared to the length scale characterizing the material's microstructure. However, when the geometries of critical dimensions on a device approach the size of material's microstructure, the size effects prevail, and the bulk properties can no longer be used to predict mechanical behaviour.

Nowadays, the size effects in plasticity are well-known: smaller samples are consistently reported to be stronger than their bulk counterparts, and plastic deformation in small volumes requires the application of higher stresses [1-23]. Some of the mechanisms responsible for strengthening in thin films, for example, are well understood and can be attributed to grain size hardening, the confinement of dislocations within the film by the presence of the substrate and in some cases, the passivation, or to the presence of strong strain gradients. Following the nomenclature in the review by Nix, *et al.* [20], this type [21] size effects arises from the constraining effects of the surrounding layers or from the microstructures present in these thin films and are classified as *extrinsic*. The *intrinsic* size effects are those that arise when single crystals are deformed in small, unconstrained volumes, and the operating deformation mechanisms appear to be a matter of on-going discussion.

In this article, we focus our attention on size effects arising in uniaxial deformation of crystals. In this configuration, a uniform top load is applied to a single crystalline sample of *sub-micron* dimensions, whose initial dislocation density is on the order of $10^{12}/m^2$. This particular type of deformation is chosen because the material is not expected to

Corresponding author: Julia R. Greer, e-mail: jrosolov@alum.mit.edu

strengthen through one of the known mechanisms like strain gradient plasticity, dislocation confinement, grain size hardening, or initial lack of dislocations. Moreover, several recent studies suggest that a fundamentally different plasticity mechanism might operate when the sample dimensions are similar to its microstructure [19-23]. As the capabilities of experimental techniques advance ever closer to linking the specimen dimensions with those of computational cells, it is useful to compare some of the results of atomistic simulations to real-life systems. To illustrate this, we present a brief review of some of the computational findings addressing plasticity mechanisms in uniform deformation and compare them with our experimental results on micro-compression of gold nanopillars, fabricated by using Focused Ion beam (FIB) machining. These sub-micron free-standing cylinders were found to plastically deform in uniaxial compression reaching stresses as high as 800 MPa, corresponding to ~ 50% of theoretical shear strength of gold[1]. We present in detail a phenomenological model attributing such behaviour to *hardening by dislocation starvation*, unique to very small crystals. The physical premise of the model is that during deformation, mobile dislocations have a higher probability of annihilating at a nearby free surface than of interacting with other dislocations and forming sessile junctions. When the starvation conditions are met, plasticity is accommodated by the nucleation and motion of new dislocations rather than by motion and interaction of existing dislocations, as is the case for bulk crystals.

2. STRENGTHENING BY PERCOLATION

Based on an extension of the 'areal glide' model of Kocks [24] and on the observation of common fractal dimensions between percolating dislocations and fluids, Gil Sevillano, *et al.* [25] interpreted plastic yield as a phenomenon analogous to invasion-percolation in fluids. In this model, percolation physically involves an 'invading finger' of the dislocation line that locally defeats the obstacle array, rather than a self-similar advancing uniform dislocation front that defeats all obstacles. Two-dimensional dislocation glide through a field of discrete obstacles is analogous to 2-D invasion percolation of a fluid through a porous medium, as the local mechanisms are identical. Both processes display a percolation-unpinning transition at some critical contact angle, ϕ_c, and some obstacle strength. The transition separates the obstacle bowing-out Orowan regime of dislocation advance from the obstacle-cutting Friedel regime of advance by un-zipping. The main hypothesis of the percolation theory is that when dislocations percolate through a forest of strong obstacles, the following relationship holds between the normalized stored dislocation line length at the percolation stress, the scaled samples size, and the percolation stress:

$$\frac{L_\rho(\tau, D)}{L^{D_e}} = g_\rho \times \left(L^{1/\nu} \frac{\tau - \tau_c}{\tau_c} \right), \qquad (1)$$

where L is the linear size of the simulation cell ($L \times L$ square in the simulation cell), L_ρ is the length of the gliding dislocation, $D_e = 4/3$ is the fractal dimension of the dislocation line, $\nu = 4/3$ is the exponent of the correlation length, τ is the percolation stress, or critical resolved shear stress (CRSS) of the given sample, τ_c is the CRSS for the infinite sample, and g_ρ is the scaling function. The size effect in percolation transitions is then as follows: when the size of the system, L, is well above the characteristic length, no size effects are expected, and the average lengths will scale with the system size: $L_\rho \propto L$. However, when the size of the system becomes compatible with the characteristic length, the scaling is expected to vary with fractal dimension: $L_\rho \propto L^{D_e}$. Based on these observations, the authors postulate that as the sample size drops below a specific critical size, the critical resolved shear stress increases through the scaling of constant α in Taylor's relation.

$$\alpha = \frac{\tau - \tau_c}{\mu b \sqrt{\rho}} \propto D^{-0.75}. \qquad (2)$$

Here, τ is the critical resolved shear stress and D is related to the sample size through the number of obstacles and the mean spacing between them. Based on this percolation theory, the size effect manifests itself through a power law dependence between the critical resolved shear stress and sample size once the sample dimensions become compatible with the characteristic percolation length.

3. MOLECULAR DYNAMICS (MD) SIMULATIONS: EMBEDDED ATOM METHOD (EAM)

Horstemeyer *et al.* [26] investigated unconstrained plasticity by performing atomistic simulations via the embedded atom method (EAM) in 2001. In these molecular dynamics simulations, the energy of embedding an atom into a computational cell is

calculated as a function of the local electron density and a repulsive pair-wise potential. The functional form of the total energy is given by:

$$E = \sum_i F^i\left(\sum_{i\neq j}\rho^i\left(r^{ij}\right)\right) + \frac{1}{2}\sum_{i,j}\phi^{ij}\left(r^{ij}\right), \quad (3)$$

where *i* refers to the atom in question and *j* refers to the neighboring atom, r^{ij} is the separation distance between those atoms, and φ^{ij} is the pair potential. These atomistic simulations were performed in simple shear at 300K for systems containing between 100 and $100\cdot10^6$ atoms in pristine crystals. The geometries of deforming volumes were likened to that of a wire, a flat sheet, and a sample with low- and high-angle grain boundaries. The yield stresses were then calculated based on the volume average of these forces in response to a known shear deformation. The common length scale parameter was the ratio of the volume to the surface area of the sample. Results of these molecular dynamics simulations revealed that plastic deformation is intrinsically inhomogeneous, that the yield strength depends on the sample size even in the absence of strain gradients, and that for small single crystals, the yield strength scales inversely with the *volume-to-surface area ratio* of the sample. While this result is encouraging, the boundary conditions on the computational cell are set up in such a way that the sample yields when the initial dislocations are necessarily emitted from the surface because of *the local stress gradients* in the corners. Imposing such boundary conditions inherently forces the sample to yield at the specific points where the stress concentrations are much higher than elsewhere in the sample.

Another example of utilizing the Embedded Atom Method to investigate nucleation-controlled plasticity was published in 2005 by Zuo *et al.* [27]. In their simulation model, the authors used the EAM approach to a small computational cell subjected to homogeneous shear. It was found that atoms whose relative displacements are higher than 1/2 of the Shockley partial vector formed clusters, or 'hot zones', resulting in the creation of Shockley partial dislocation loops. The fraction of atoms with higher displacements obeys the Weibull distribution, and the mean relative displacement of the atoms, $\langle x\rangle$, is directly proportional to x_0, a linear function of shear strain, γ, resolved onto the slip system:

$$x_0 = A(T)\gamma + B(T), \quad (4)$$

where $A(T)$ and $B(T)$ are functions of temperature only, corresponding to the atomic displacements in the direction of the applied strain and the more randomized thermally-activated jumps, respectively. Calculating the probability that any given atom within the volume will attain the critical displacement to form a nucleation site enables for determination of the critical distance, $x_{critical} = \alpha a_0 / \sqrt{6}$, where α is predicted by EAM to be 0.478 rather than 0.5. When an atomic displacement is less than this critical value, additional thermal agitation is required to achieve this critical distance. The following expression for the elastic shear strain, γ, is obtained:

$$\gamma = \frac{1}{A(T)}\left\{a_0\left(\frac{\alpha}{\sqrt{6}} - \beta(\gamma,T)\right) \times \ln(N)^{-\frac{1}{m}} - B(T)\right\}, \quad (5)$$

where β represents the additional thermal agitation component and is a function of the strain rate and temperature. The size effect is prevalent, as the nucleation stresses are a function of the number of atoms, *N*.

4. DISLOCATION DYNAMICS (DD) SIMULATIONS: DISLOCATION SOURCE STARVATION

More recently, a discrete dislocation plasticity analysis was performed by Deshpande *et al.*, who investigated the effect of size and loading conditions on the tensile and compressive behavior of micron-sized planar crystals [28]. In their model, such parameters as dislocation drag, obstacle interactions, and dislocation nucleation and annihilation are incorporated through a set of constitutive rules. The authors found that under unconstrained tensile axis boundary conditions, the flow strength increased with decreasing specimen size and that below a certain size, the flow strength of the crystals is set by the nucleation strength of the initially present Frank-Read sources. For the range of lateral dimension, *W*, varying between 0.75 μm and 4 μm, the relationship between flow stress and size was found to obey the following power law:

$$\sigma_f = \alpha\left(\frac{W}{W_0}\right)^{-0.49}, \quad (6)$$

where W_0 = 1 μm is a reference size and α is a constant on the order of 67 MPa. While this power

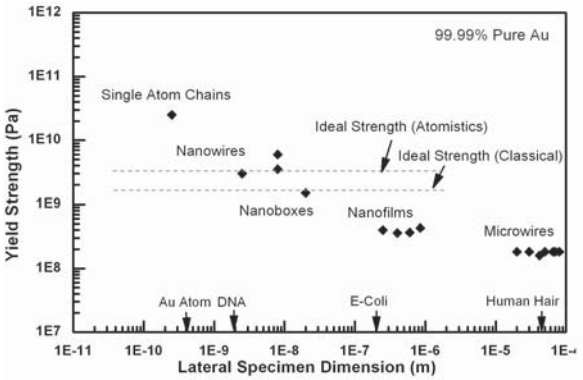

Fig. 1. Ideal predictions and experimental measurements regarding the yield strength of 99.99% pure Au as a function of lateral specimen dimension. The data show a systematic trend toward stronger materials as the size is reduced towards atomistic scale. At discrete experimental length scales, the materials in the nanometer and micrometer range all demonstrate yielding, while single-atom chains undergo atomic separation. The relative sizes of various natural substances are included for reference.

law fits the computed strengths in the intermediate size regime very well, there exist an upper and lower plateaus of the flow strengths. The smaller specimens, whose lateral dimensions are less than 0.4 μm have a flow strength proportional to the dislocation nucleation shear stress, which is a constant for a given material:

$$\sigma_f \approx \frac{2\tau_{nucl}}{\sin 2\phi} \qquad (7)$$

In these calculations the dislocation source density was independent of the sample size, so smaller samples inevitably contained fewer Frank-Read sources, giving rise to an increase in strength. Additionally, in small specimens, the mean-free path of mobile dislocations becomes shorter than the distance between the obstacles inside the sample, enabling the dislocations to escape the crystal, leaving it starved of dislocation sources. Nucleation of new dislocations is then required for further plastic deformation.

5. NUCLEATION-CONTROLLED DISLOCATION DYNAMICS SIMULATIONS

The yield strength of gold nanowires was investigated via atomistic simulations by Gall *et al.* [29]. The atomistic predictions of strength were found to be quantitatively consistent with discrete experimental measurements and revealed the mechanisms for increasing nanowire strength with decreasing dimensional scale. Some of the conclusions were that the nanowire strength is considerably higher than bulk materials, that it depends on the diameter of the wire, and that it cannot be predicted by the ideal bulk strength theories. The key contributors to the mechanism of strengthening at the nanometer scale were found to involve the scarcity and low mobility of dislocations coupled with the constraints from the surface stresses. The presence of free surfaces leads to the formation of intrinsic compressive stresses and dislocation-resistant wire structures, which drive the increase in the tensile yield strength. Additionally, free surfaces were found to serve as favorable nucleation sites for defects in perfect nanowires, also resulting in the tensile yield strength increase. A collection of experimental yield strength measurements on 99.99% pure gold is presented in Fig. 1 as a function of the lateral specimen dimension.

6. THEORETICAL SHEAR STRENGTH

The plot also shows that for lateral specimen dimensions below ~50 nm, the predicted yield strengths are on the order of the theoretical shear strength predictions. Therefore, it is useful to consider the stresses required to nucleate new dislocations. The classical Frenkel method, for example, assumes a sinusoidal dependence between the shear stress and the distance a crystallographic plane moves with respect to its neighbors. Kelly, in his book 'Strong Solids', [30] expanded this method to account for the low stacking fault energy of gold and for the distortion of the atomic planes as they slide past each other and determined the ideal theoretical *shear* strength of gold, τ_{max} to be 0.74 GPa. The *classical* prediction of the ideal theoretical yield strength in Fig. 1 is calculated based on Kelly's method. The theoretical *axial* yield strength of 1.48 GPa corresponding to this shear strength, represents the 'lower limit' since single crystals show anisotropy, and the orientation of the preferred slip planes most likely is different from 45°. Gall's atomistic predictions are based on bulk simulations, periodic in all directions, of shearing two Au {111} planes in <112> directions. A <112>-type direction is chosen over a <110>-type because it is more energetically favourable for a {111} plane in FCC crystal to slide in two steps, following the <112> Shockley partials, rather than in a single slip step.

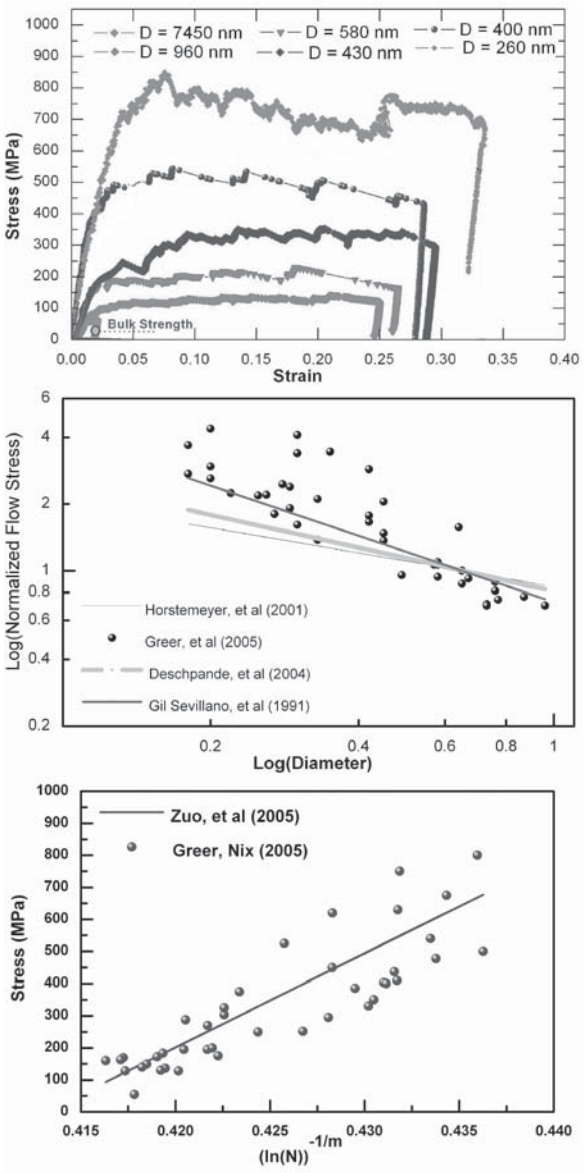

Fig. 2. (a) Stress vs. strain for <001>-oriented FIB gold pillars, whose diameters range from several microns to 260 nm. (b) Log-Log plot of normalized flow (yield) stresses as a function of lateral dimensions for computational studies reviewed in this paper compared with the experimental data, and (c) The stresses predicted by Zuo, et al. are plotted vs. length characteristic related to the number of atoms in the sample, as compared with our experimental findings.

These atomistic calculations predict the *axial* ideal theoretical yield strength to be on the order of 3 GPa and is considered to be an upper bound on the yield strength since it is based on the coordinated shearing of two adjacent atomic planes in the absence of defect nucleation from surfaces or structural inhomogeneities. In 2004, Ogata *et al.* [31] used density functional theory (DFT) to analyze the stress-strain responses of 22 metals and ceramics to determine the maximum shear strain that a homogeneous crystal can withstand. They confirmed that the Frenkel model for ideal shear strength works well for both metals and ceramics when shearability is taken into account and used in the scaling. The shearability of metals was found to correlate with the degree of valence charge localization and with directional bonding. They further tabulated the shear moduli, ideal shear strains and stresses for all the studied materials. This most recent study reveals the gold's ideal shear strength to be 850 MPa, which closely matches the value based on the Kelly analysis (740 MPa). While much progress has been made in estimating materials' ideal shear strength, most studies do not take into account the atomistic nature of nucleating a dislocation near a *free surface*, where the values of theoretical strength are expected to be lower. Therefore, in the presence of free surfaces, the fraction of applied stress to the theoretical strength is expected to be higher, activating nucleation-controlled plasticity.

This brief review of recent computational work in plasticity at the nano-scale shows that there are several rather different approaches explaining the observation of higher strengths in smaller volumes of material when not constrained by surrounding materials. Only recently, plasticity theories started concentrating on considering changes to the fundamental deformation mechanisms associated with the size reduction like the dislocation mean-free path, glide sources, dislocation travel distances, *etc*. Although the results of studies are unified in the tenet that 'smaller is stronger', the explanations for the deformation mechanisms vary greatly. In the next section we present experimentally-determined stresses of gold nanopillars and compare them with the aforementioned models.

7. SIZE EFFECT IN GOLD NANOPILLARS

The uniaxial compression procedure and methodology for stress-strain calculations, as well as the FIB fabrication technique are described in detail elsewhere [22]. The results of our uniaxial compression experiments indicate a strong sample size effect: the flow stresses for gold pillars are much higher than the typical strength of bulk gold, estimated at 20 MPa at 2% strain [32]. Moreover, the flow stresses for single-crystalline <001>-oriented pillars

increase from ~50 MPa to 800 MPa as the diameter is reduce from several microns to on the order of 200 nm. A set of some stress-strain curves from compressions of <001>-oriented gold pillars, as well as the log-log plot of normalized pillar stresses in comparison with model predictions, are shown in Fig. 2.

An interesting feature of the stress-strain curves for nanometer-sized pillars shown in Fig. 2a is the apparent lack of the Stage II work-hardening region associated with the activation of multiple slip systems in the course of deformation of single crystals. Contrary to this, the stress-strain behavior agrees more with the Stage I-type deformation, or the 'easy glide' section of a low-symmetry oriented single crystal deformation curve. Moreover, a representative stress-strain curve in this work is composed of a number of discrete slip events separated by elastic loading segments, while the overall stress level remains nearly constant as the strain increases. This suggests that the hardening mechanism here is quite opposite from the conventional strain-hardening, with the elastic loading sections indicative of the *absence* of dislocations rather than their multiplication. The experiments also revealed that the strength increase was consistent with the overall power-law dependence, as can be seen from the Log-Log plot in Fig. 2b. However, the rate at which the stresses increase as a function of length scale appears to be higher than those of computational studies, on the order of -1. This finding shows that deformation at the sub-micron scale does not obey conventional plasticity mechanisms and supports the argument for the lack of dislocations in the deformed sample. It should be noted that while Fig. 2c shows a close agreement between the data and Zuo *et al.*'s atomistic simulations, the MD simulation was performed for the deformation of Ni_3Al, and several parameters had to be modified in order to achieve the best fit for gold.

Due to the novelty of these experiments at the time and to the unusually high stresses sustainable by single-crystal gold, we performed a thorough analysis addressing the possibilities of experimental factors contributing to the observed behavior. Some of these include Ga^+ contamination from the FIB source, axial misalignment between the specimen and the indenter, end constraints of the chosen pillar geometry, and non-uniformity of the actual pillar deformation. We were able to show that although some Ga^+ ions from FIB processing were congregated in the surface layer, the presence of a thin surface layer does not appear to be a major

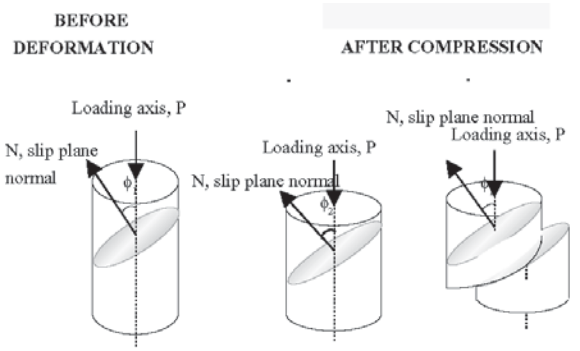

Fig. 3. Deformation behavior of a cylinder in uniaxial compression in fully (a) constrained and (b) unconstrained cases. Before deformation, the angle between the loading axis and the slip plane normal is ϕ_1. After deformation takes place, in the constrained case the normal *N* is rotated away from the loading axis, and the new angle is ϕ_2. In the case of compression, $\phi_2 > \phi_1$ (this would be the opposite for the case of tension). In the unconstrained case, the angle ϕ_1 remains the same while the pillar loses its shape.

contributing factor in the observed strength increase [23]. While axial misalignment remains a possibility, very high bending angles would be required in order to attain the order of magnitude of the observed stresses. As mechanics community is engaging in similar micro-compression experiments, a set of guidelines for the design of accurate micro-compression experiments was recently reported by Zhang *et al.* [33]. They conclude that the required aspect ratio of the pillars has to be no greater than 5 to avoid buckling, that the taper of the pillar results in overestimation of the elastic modulus, and that misalignment of the specimen significantly affects the test's accuracy. Here we show that the end constraints of the cylinder do not appear to play a major role at the strains of interest.

In FCC crystals, loading in a high-symmetry orientation causes multiple slip systems' activation, resulting in a more homogeneous deformation upon uniaxial compression. Uniaxial loading in the <001> direction, chosen for our experiments and corresponding to a high-symmetry orientation, would result in the activation of twelve different $\{111\}/<01\bar{1}>$ slip systems, with the pillar deforming uniformly around its diameter as it is compressed. In this orientation, despite the presence of the end constraints, the pillar remains centrally-loaded and preserves its cylindrical shape throughout the de-

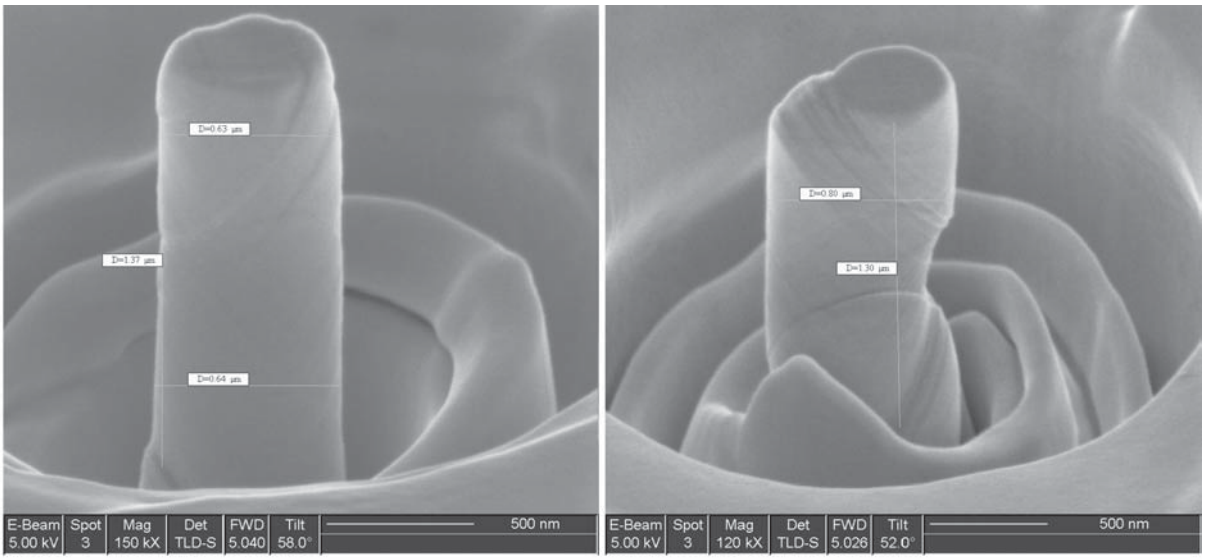

Fig. 4. SEM images of two deformed pillars. The image on the left corresponds to a pillar after 15% compression whose deformation was homogeneous and occurred on multiple slip systems, while the image on the right shows a different pillar, where plastic deformation occurred preferentially on only one set of crystallographic planes.

formation process. If, in the course of deformation, only one slip system is activated, and if the ends of the deforming cylinder are *constrained*, or rigidly attached, the orientation of the active slip system relative to the loading axis changes. The position of the compressive axis will move until a higher-symmetry orientation is reached, when another slip system will be activated. If the ends of the cylinder are *unconstrained,* or are free to move laterally in the course of deformation, the orientation of the loading axis with respect to the slip plane normal remains constant and the pillar loses the integrity of its shape. A schematic of two extreme cases for the constraints of the top and the bottom of the cylinder in compression when only a single slip system is active is shown in Fig. 3.

While the surface steps formed by slip processes in a single slip system can be easily observed and analyzed, the disadvantage of studying mechanical properties in a low-symmetry orientation is that regardless of the constraints, the deformation is inhomogeneous, which results in the development of stress concentrators at the deformed edges, as shown in the SEM images in Fig. 4. Such configurations would prevent a precise calculation of the cross-sectional area needed for the determination of true stress.

The slip lines on the deformed specimen are oriented at approximately 55° from the loading axis matching the calculated value of 54.7° as the angle between <001> and <111> zone axes. In order to address the effects of constraints on the observed strengths, the stresses arising during uniaxial compression of gold in both the fully *constrained and fully unconstrained* cases were compared. For the former, an FEM simulation of 50% compression was performed using a theoretical stress-strain curve, assuming a fully elastic behavior until the yield stress of 89 MPa, followed by the work-hardening segment at the rate of $E_{gold}/300$, or 0.263 GPa. The initial geometry of the pillar was chosen in accordance with the 3:1 aspect ratio. This simulation generated a set of load-displacement data based on the theoretical stress-strain curve. Subsequently, treating this load-displacement data generated by the FEM as “experimental” and converting it to stresses and strains based on our methodology generated a stress-strain curve corresponding to the *unconstrained* loading conditions. This comparison is presented in Fig. 5, where the ratio of the two stresses is plotted as a function of plastic strain. It is clear from this plot that until approximately 25% strain, the difference in stresses due to the constraint effects is less than 10%, showing convincingly that

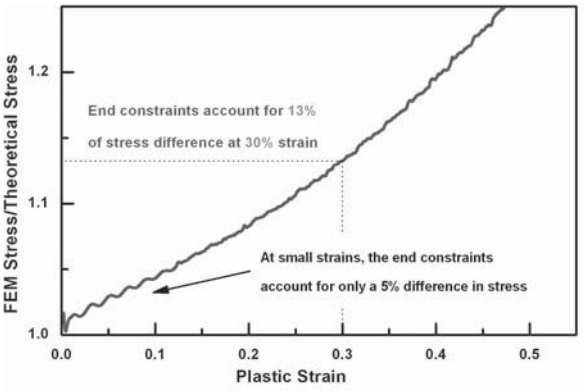

Fig. 5. Ratio between the stresses in the unconstrained and constrained cases plotted as a function of plastic strain. The effects of end constraints account for no more than 5% of the stress up to approximately 10% strain and become significant after the sample has been deformed by 1/3.

the constraint effects do not appear to play a significant role in the observed size effect.

8. DISLOCATION STARVATION

These observed great strengths of gold in uniaxial compression do not appear to be due to the presence of a surface layer associated with a particular fabrication technique, nor are they due to the particular end constraints. Post-deformation TEM images revealed no evidence of cellular dislocation network formation, characteristic of the conventional strain-hardening [34]. Finally, preliminary X-ray microdiffraction studies indicate that they are not likely to be due to the presence of strain gradients [35]. Therefore, the plasticity mechanism in this case is a pure function of sample size and geometry. Therefore, a more appropriate explanation for these high strengths can be based on the concept of *dislocation starvation*. One might argue that in these sub-micron-sized samples, any dislocation is in the vicinity of a free surface, where it can annihilate and reduce the overall dislocation density. If we assume that for a pillar of radius *a*, any dislocation found within distance *vdt* from a free surface has a 50% probability of escaping the crystal, the dislocation annihilation rate is an inverse function of the pillar size as follows:

$$d\rho^{-} = -\rho\left(\frac{1}{2}\frac{2\pi a v dt}{\pi a^2}\right) = -\rho\frac{v dt}{a}, \qquad (8)$$

where *v* is the dislocation velocity. In this configuration, any mobile dislocation or its partial is more likely to escape the crystal than to elastically interact with other dislocations or to replicate itself. The dislocation multiplication rate is related to the breeding coefficient, δ, or the inverse of the distance a dislocation will travel before replicating itself [36]:

$$d\rho^{+} = \rho\delta v dt. \qquad (9)$$

The overall rate of dislocation density is the sum of dislocation multiplication and dislocation annihilation rates; the total dislocation density then evolves in the following way:

$$\rho = \rho_0 + \frac{(\delta - 1/a)}{b}\cdot\frac{\varepsilon_p}{M}, \qquad (10)$$

where ε_p is the axial plastic strain, *b* is the Burgers vector, and M = cosλcosϕ is the Schmid factor involving the angles λ and ϕ, denoting the slip direction and slip plane normal relative to the axis of deformation. Based on Eq. (10), it is clear that if the crystal is smaller than the reciprocal of the breeding coefficient, the overall dislocation density would decrease in the course of deformation. Therefore, unlike in conventional plasticity, at the nano-scale, the rate of dislocation accumulation is lower than that of dislocation annihilation, requiring the nearly perfect crystal to sustain the close-to-theoretical stresses in order to accommodate further plasticity. A useful form for the relationship between the applied shear stress and the dislocation velocity is also modelled after Gilman:

$$v = \frac{\tau}{B}\exp\left(\frac{-20\tau_{resist}}{\tau}\right), \qquad (11)$$

where τ is the applied shear stress, $B = 3\cdot10^5$ Pa·s/m is the drag coefficient, and τ_{resist} is the average resistance stress arising from elastic interactions of dislocations and the bowing force on dislocations moving across the pillar. The stress arising from the elastic interactions between dislocations can be represented by the conventional Taylor hardening:

$$\tau_{dislocation} = \frac{1}{2}\mu b\sqrt{\rho}\,. \qquad (12)$$

Another component of the resistance stress stems from dislocation bowing, as it travels from the surface of the pillar to the middle. To achieve the lowest-energy configuration, the dislocation line orients itself normal to the free surfaces throughout its travel. As a dislocation with line tension Γ travels across

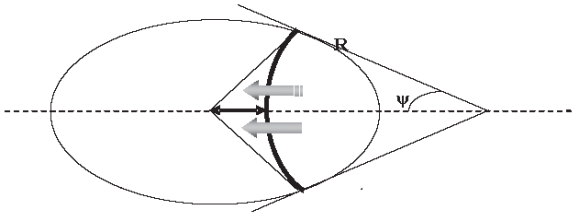

Fig. 6. A schematic of a dislocation segment gliding in its {111} slip plane, lengthening itself and bowing out as it traverses from the surface of the pillar towards its middle.

an elliptical crystal cross-section of a {111}-type slip plane, which passes through $\{0,\alpha\}$ and $\left\{\sqrt{3/2}a, 0\right\}$, the schematic in Fig. 6 can be used to illustrate this geometry[2]:

The bowing stress of a dislocation is related to the dislocation line tension, Γ, through the dislocation bowing radius, R:

$$\tau \cdot b = \frac{\Gamma}{R}. \tag{13}$$

Here, the bowing stress τ is a function of s, the distance between the dislocation and the centre of the pillar. The expression for the dislocation line tension is, approximately,

$$\Gamma = \frac{\mu b^2}{4\pi(1-\nu)} \ln\left(\frac{\alpha a}{b}\right), \tag{14}$$

where α is a constant of order unity. Solving for the geometry depicted in Fig. 6, the radius of curvature of the dislocation line can be expressed in terms of the fractional distance between the dislocation line and the pillar center, (s/a), in the following way:

$$R = a \cdot \frac{\left(1-(s/a)^2\right)}{2\cdot(s/a)}. \tag{15}$$

The average resistance stress, $\bar{\tau}$, is then simply the ratio of $\int_0^a \tau \cdot R\psi ds$ and $\int_0^a R\psi ds$, or the average stress integrated the over the cross-sectional area swept by the gliding dislocation. Combining these equations, the expression for the *total average resistance shear stress* that any mobile dislocation has to overcome in order to glide in its plane is:

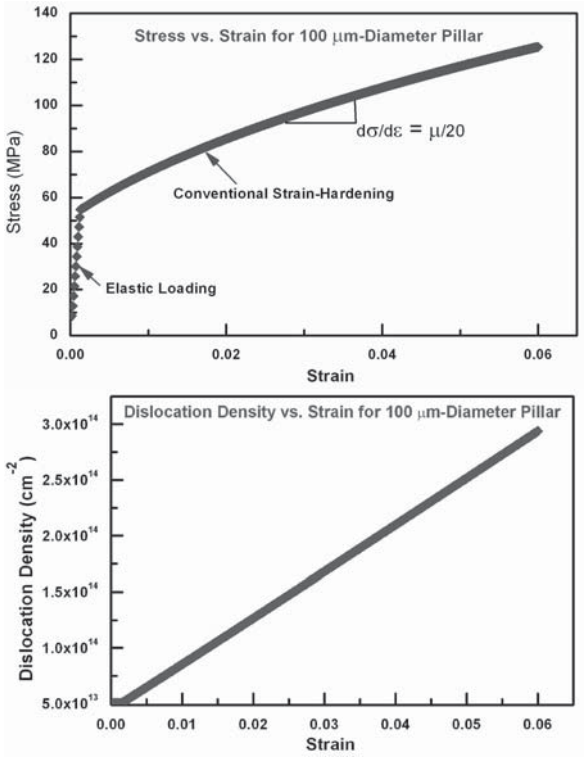

Fig. 7. (a) Stress vs. strain model predictions for a larger pillar with a 100 μm diameter. (b) Dislocation density vs. strain model predictions for a larger pillar with a 100 μm diameter. The dislocation density clearly increases linearly in the course of plastic deformation.

$$\tau_{resist} = 0.5\mu b\sqrt{\rho} + 1.4\frac{\mu b}{4\pi a(1-\nu)} \ln\left(\frac{\alpha a}{b}\right), \tag{16}$$

where μ is the elastic shear modulus and ν is Poisson's ratio. Determination of this resistance stress enables us to iteratively calculate the dislocation velocity according to Eq. (11). From the velocity, v, the dislocation density, ρ, and the Burgers vector, b, the expression for the overall rate of strain can be developed as a sum of the elastic and plastic components, respectively:

$$\dot{\varepsilon} = \frac{1}{E}\frac{d\sigma}{dt} + \frac{\rho b v}{M}. \tag{17}$$

Fixing a constant strain rate allows us to numerically calculate the stresses and strains at each increment in time. Table 1 provides a schematic de-

Table 1. Step-by-step numerical calculation algorithm of the dislocation starvation model.

Step 1. Assign initial values.	Initial dislocation density, $\rho_0 = 5 \cdot 10^{12} m^{-2}$, Burgers vector, $b = 3 \cdot 10^{-10} m$, Breeding coefficient, $\delta = 7 \cdot 10^{5} m^{-1}$, Schmid factor, $M = \cos\lambda \cdot \cos\phi = 1/\sqrt{6}$, Initial strain, $\varepsilon_0 = 0.0001$, Constant strain rate, $\dot{\varepsilon} = 0.0001 s^{-1}$, Increment in strain, $\Delta\varepsilon = \dot{\varepsilon} \cdot \Delta t = 0.0001$
Step 2. Establish relationship between **axial** and **shear** stresses.	$\sigma = \tau/\cos\lambda \cdot \cos\phi = \tau/M$
Step 3. Express instantaneous pillar **diameter** as a function of axial strain.	$a_i = a_0 \cdot \sqrt{L_1 / L_0} = a_0 e^{0.5}$, where L_0 is the initial height, L_i is the instantaneous height of the pil lar at time step *i*, and ε_i is the axial strain.
Step 4. Calculate **plastic strain** by subtracting the elastic component from total strain.	$\varepsilon_{plastivc,i} = \varepsilon_i - \sigma_i/E_{<xyz>}$ where $E_{<xyz>}$ is the elastic modulus in the specific <*xyz*> crystallographic orientation. **Note**: for the first step, s_0 is simply elastic, or $\sigma_0 = \varepsilon_0 \cdot E_{<xyz>}$
Step 5. Calculate **dislocation density.**	$\rho_i = \rho_0 + (\delta - 1/a_i)/b \cdot \varepsilon_{plastivc,i}/M$
Step 6. Calculate dislocation **resistance shear stress**·	$\tau_{resistance,i} = 0.5\mu b\sqrt{\rho_i} + 1.4\dfrac{\mu b}{4\pi a_i(1-\nu)}\ln\left(\dfrac{\alpha a_i}{b}\right)$
Step 7. Calculate **resolved shear stress**.	$\tau_i = \sigma_i M$
Step 8. Calculate **dislocation velocity.**	$v_i = \dfrac{\tau_i}{B} \cdot \exp\left(\dfrac{-20\tau_{resistance,i}}{\tau_i}\right)$
Step 9. Finally, from dislocation density (Step 5) and dislocation velocity (Step 8), calculate an increment in **axial stress**.	$\Delta\sigma = E_{<xyz>} \cdot \Delta\varepsilon\,(1 - \{M \cdot \rho_i b v_i/\dot{\varepsilon}\})$
Step 10. Update stress and strain values for the (i+1)st time increment and repeat the procedure starting from Step 3.	$\sigma_{i+1} = \sigma_i + \Delta\sigma$ $\varepsilon_{i+1} = \varepsilon_i + \Delta\varepsilon$

picting the iterative numerical algorithm for calculating the evolving dislocation density and the corresponding stresses and strains by locking a constant strain rate.

For large sample sizes, for example, 100 μm, the shape of the stress-strain curve generated by this procedure is consistent with conventional strain-hardening behaviour: dislocations elastically interact with each other and form sessile dislocations, for example, Lomer-Cottrell locks, which act as obstacles to the motion of other gliding dislocations. More and more dislocations get pinned by these locks, forming Frank-Read sources, causing the total number of dislocations to increase. Both stress and dislocation density are plotted in Fig. 7 as a function of increasing plastic strain.

Quite to the contrary, the stress-strain behaviour of a 500 nm-diameter pillar, where $a<1/\delta$, is characterized by initial elastic loading, a region of declining flow stress, followed by abrupt elastic loading when the crystal becomes dislocation starved. As the mobile dislocations escape at a nearby free surface, the dislocation density is rapidly reduced, and the dislocation-starved conditions are attained. This concept of dislocation starvation is illustrated in Fig. 8, where the model-generated stress-strain and dislocation density are plotted vs. strain.

It is very clear from the comparison of stress/strain graphs above that by the time the pillars are deformed by 7%, the stress level supported by the smaller pillar is at least 3 times higher than that for the larger one. It is important to recognize that this model focuses *only* on the starvation process and does not incorporate any possible dislocation nucleation events. It simply shows that for crystals below a critical size, $1/\delta$, the dislocation density should

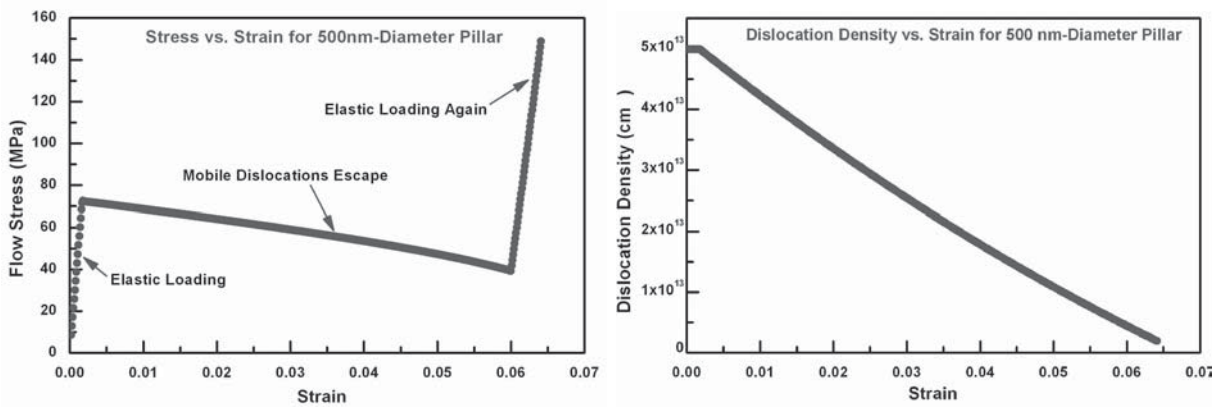

Fig. 8. (a) Stress vs. strain model predictions for a smaller pillar with a 500 nm diameter. After elastic loading, the mobile dislocations escape at the nearby free surfaces, thereby reducing the dislocation density, and the crystal becomes dislocation-starved. (b) Dislocation density vs. strain model.

decline in the course of deformation and tend toward a dislocation-starved state. When such a state is reached, the stress would be expected to rise abruptly leading subsequently to the nucleation of new dislocations. While the dislocation starvation model presented here does not encompass physical phenomena like possible dislocation interactions with point defects, nucleation of new dislocations, and time-dependent processes, it is consistent with the Transmission Electron Microscopy (TEM) analysis [23]. This concept of dislocation starvation naturally leads to the need for determination the fraction of ideal strength these pillars are able to sustain. Based on the earlier discussion, our analysis revealed that the theoretical *axial* yield strength of gold is 1.65 GPa, making the maximum stress of 850 MPa for the smallest pillar of ~200 nm be on the order of 45% of gold's theoretical strength. Xu and Argon [37] showed that when a perfect crystal is subjected to applied stress, the activation energy required for nucleation of dislocation loops is a strong decreasing function of the ratio of the applied shear stress and the ideal shear strength. The stress levels attained for our smallest pillars correspond to $\sim 0.45\tau_{theoretical}$, requiring a high energy of 13.26 eV to homogeneously nucleate a dislocation loop. Based on this argument, the stresses arising in our pillars are too low for homogeneous dislocation loop nucleation. However, when the presence of free surfaces and the atomistic nature of dislocation creation are incorporated in the determination of the ideal strength, the fraction of applied stress to the theoretical strength will be higher, requiring lower, more realistic energies to activate nucleation.

9. SUMMARY

Following the advancement of possible experimental techniques, it is becoming possible to link computational models with real-life observations of size effects associated with the scale of plastic deformation. To illustrate this, we reviewed the results of several previously reported molecular and dislocation dynamics simulations as well as of hardening by percolation and compared them with our experimental data from uniaxial compression of gold nanopillars fabricated by using Focused Ion beam (FIB) machining. All computational studies postulate a power-law dependence between the yield stress and the sample dimensions when subjected to uniform deformation, with smaller sizes resulting in higher strengths. The power constants in these studies varied from -0.38 to -0.75, with the higher value corresponding to Gil Sevillano's percolation theory. While the overall power correlation is also present in the experimental data, the slope of the stress increase appears to be much higher, on the order of -1. Also, the experimentally-determined stresses for the smallest sample reach as high as ~50% of theoretical shear strength of gold, suggesting that a fundamentally different plasticity mechanism might operate when the sample dimensions are similar to its microstructure.

The interpretation of the observed behaviour might be explained by the phenomenological model of

hardening by dislocation starvation, presented here in great detail. It is important to recognize that this model focuses *only* on the starvation process and does not incorporate any physical phenomena like possible dislocation reactions with point defects, nucleation of new dislocations, or time-dependent processes. It convincingly shows, however, that for crystals below a critical size, the dislocation density should decline in the course of deformation and tend toward a dislocation-starved state, requiring subsequent elastic-type loading until a new dislocation is nucleated.

REFERENCES

[1] H.D. Espinosa and B.C. Prorok // *J. Mat. Sci.* **38** (2004) 4125.

[2] L. Nicola, E. Van der Giessen and A. Needleman // *J. Appl. Phys* **93** (2003) 5920.

[3] W.W. Gerberich, J.M. Jungk, M. Li, A.L. Volinsky, J.W. Hoehn and K. Yoder // *Int. J. Fracture*. **119** (2003) 387.

[4] Q. Maand D.R. Clarke // *J. Mater. Res*. **10** (1995) 853.

[5] A.L. Shull and F. Spaepen // *Current Opinion in Solid State and Materials Science* **1** (1996) 679.

[6] W.J. Poole, M.F. Ashby and N.A. Fleck // *Scripta metal. et mater*. **34** (1996) 559.

[7] A.A. Benzerga, V. Tvergaard and A. Needleman // *Int. J. of Fracture* **116** (2002) 275.

[8] H. Espinosa, S. Berbenni, M. Panico and K. Schwarts // *PNAS* **102** (2005) 16933.

[9] K.W. McElhaney, J.J. Vlassak and W.D. Nix // *J. Mater. Res.* **13** (1998) 1300.

[10] S. Suresh, T.G. Nieh and B.W. Choi // *Scripta Mater*. **41** (1999) 951.

[11] W.W. Gerberich, N.I. Tymiak, J.C. Grunlan, M.F. Horstemeyer and M.I. Baskes // *J Appl Mech – Trans ASME* **69** (2002) 433.

[12] Y. Huang, H. Gao, W.D. Nix and J.W. Hutchinson // *J. Mech. Phys. Solids* **48** (2000) 99.

[13] B. Schuster, Q. Wei, H. Zhang and K. Ramesh // *Appl. Phys. Lett.* **88** (2006) 103112.

[14] E. Arzt, G. Dehm, P. Gumbsch, O. Kraft and D. Weiss // *Prog. Mater. Sci*. **46** (2001) 283.

[15] B. von Blanckenhagen, P. Gumbsch and E. Arzt // *Phil. Mag. Lett*. **83** (2003) 1.

[16] C.V. Thompson // *J. Mat. Res.* **8** (1993) 237.

[17] G. Dehm, T. Wagner, T.J. Balk, E. Arzt and B.J. Inkson // *Journal of Mat. Sci. & Tech.* **18** (2002) 113.

[18] J. Bohm, P. Gruber, R. Spolenak, A. Stierle, A. Wanner and E. Arzt // *Rev. Sci. Instr*. **75** (2004) 1110.

[19] A. Benzerga and N. Shaver // *Scripta Mat* **54** (2006) 1937.

[20] M. Uchic, D. Dimiduk, J. Florando and W. Nix // *Science* **50** (2004) 986.

[21] W. Nix, J. Greer, G. Feng and E. Lilleodden // *Thim Film Solids* (2005) in print.

[22] J. Greer, W. Oliver and W. Nix // *Acta Mat*. **53** (2005) 1821.

[23] J. Greer and W. Nix // *Phys. Rev. B* **73** (2006) 245410.

[24] U.F. Kocks, *Dislocation Interactions: Flow Stress and Strain Hardening. Dislocations and Properties of Real Materials* (London: Institute of Metals, 1947).

[25] J. Gil Sevillano, E. Bouchaud anf L.P. Kubin // *Scripta Metall.* **25** (1991) 355.

[26] M.F. Horstemeyer, M.I. Baskes and S.J. Plimpton // *Acta Mat.* **49** (2001) 4363.

[27] L. Zuo, A. Ngan and G. Zheng // *Phys. Rev. Let*. **94** (2005) 095501.

[28] V.S. Deshpande, A. Needleman and E. van der Giessen // *Mat. Sci. and Engin.A*. (2005) in press.

[29] K. Gall, J. Diao and M. Dunn // *Nano Let*. **4** (2004) 2431.

[30] A. Kelly, *Strong Solids*, *2nd ed.* (Clarendon Press: Oxford, 1973).

[31] S. Ogata, J. Li, N. Hirosaki, Y. Shibutani and S. Yip // *Phys. Rev. B* **70** (2004) 104104.

[32] E. Savitskii, *Handbook of Precious Metals* (Hemisphere Publishing corp., 1989).

[33] H. Zhang, B. Schuster, Q. Wei and Q. Ramesh // *Scripta Mat.* **54** (2006) 181.

[34] M. Staker and D. Holt // *Acta Met.* **20** (1972) 569.

[35] A. Budiman and W.D. Nix, private communications.

[36] J.J. Gilman, *Micromechanics of Flow in Solids* (McGraw-Hill, New York, NY, 1969).

[37] G. Xu and A.S. Argon // *Phil. Mag. Lett*. **80** (2000) 605.